

Optical properties of transition metals at infrared frequencies

S. N. Rashkeev, Yu. A. Uspenskiĭ, and I. I. Mazin

P. N. Lebedev Physics Institute, Academy of Sciences of the USSR

(Submitted 12 July 1984)

Zh. Eksp. Teor. Fiz. **88**, 1687–1698 (May 1985)

The existence of direct interband transitions with $\hbar\omega \sim 0.1$ eV is considered for transition metals. As $\hbar\omega \rightarrow 0$, the degeneracy of the electron spectrum in cubic metals gives rise to a finite interband contribution to the imaginary part $\tilde{\epsilon}_2(\omega)$ of the dielectric permittivity; the corresponding contribution diverges as $1/\omega$ for metals with a hexagonal crystal structure. Moreover, $\tilde{\epsilon}^2(\omega)$ is not featureless, as is often supposed, but may have a distinct IR structure with well-defined thresholds and peaks. The dependence $\tilde{\epsilon}_2(\omega)$ is calculated numerically for the transition metals V, Nb, Mo, Rh, and Pd, and the results agree with available experimental data. The influence of low-frequency interband transitions on the error in deducing the intraband conductivity (the plasma and collision frequencies) from $\epsilon(\omega)$ is investigated numerically.

INTRODUCTION

Experimental studies of the optical properties of metals yield valuable information concerning their electronic structure and provide an easy method for measuring the dielectric permittivity $\epsilon(\omega)$. However, the interpretation of the frequency dependence $\epsilon(\omega)$ and its implications concerning the electronic structure of the metal are far from simple, particularly for the transition metals. The first step is to decompose the imaginary part $\epsilon_2(\omega) = \text{Im } \epsilon(\omega)$ into intraband and interband components:

$$\epsilon_2(\omega) = \frac{\omega_p^2}{\omega\gamma(1+\omega^2/\gamma^2)} + \tilde{\epsilon}_2(\omega). \quad (1)$$

The intraband component is described by the Drude formula and yields information on the electrons near the Fermi surface. In Eq. (1) γ is the mean collision frequency of the conduction electrons and ω_p is the plasma frequency:

$$\omega_p = (4\pi e^2 N(E_F) \langle v^2 \rangle / 3m)^{1/2} / \hbar, \quad (2)$$

where $N(E_F)$ and $\langle v^2 \rangle$ are the density of states and the mean square electron velocity on the Fermi surface. The interband contribution $\tilde{\epsilon}_2(\omega)$ is determined primarily by direct electron transitions between the bands and yields information on the electron structure within an energy interval $\sim \hbar\omega$ from the Fermi surface; the dependence $\tilde{\epsilon}_2(\omega)$ is frequently nonmonotonic. In order to decompose $\epsilon_2(\omega)$ as in (1), one usually assumes that there are no interband transitions at low frequencies $\hbar\omega \lesssim 0.5$ eV. A partial justification is provided by the analogy with monovalent metals, for which the interband absorption is known to have a threshold at energy $\hbar\omega \sim 1$ –2 eV. However, the electronic structure of the transition metals is considerably more complicated and it is far from clear that no low-frequency interband transitions are present.

The experimental results on the optical properties of the transition metals at infrared wavelengths are quite contradictory. For example, $\tilde{\epsilon}_2(\omega)$ was found to have a peak at $\hbar\omega \approx 0.3$ eV for niobium in Ref. 1, whereas the low-frequency dependence $\tilde{\epsilon}_2(\omega)$ was completely featureless in Ref. 2. It was noted more recently in Ref. 3 that $\epsilon_2(\omega)$ differs appreciably from the Drude result even for $\hbar\omega \sim 0.1$ eV. There is a similar disagreement in the experimental results for vanadi-

um and tantalum,^{3,4} rhodium,^{5,6} and various other transition metals. By contrast, all the experiments indicate that the IR dependence $\tilde{\epsilon}_2(\omega)$ for molybdenum is featureless.^{3,4}

Numerical calculations of $\epsilon(\omega)$ can provide valuable insight into the optical properties of metals. Unfortunately, few such calculations have been carried out, and even fewer cover the low-frequency range. It was found in Ref. 7 that $\tilde{\epsilon}_2(\omega)$ has a peak at $\hbar\omega \approx 0.2$ eV for niobium, while $\tilde{\epsilon}_2(\omega)$ tends smoothly to zero as $\hbar\omega \rightarrow 0$ for molybdenum. The calculations in Ref. 8 revealed that there is no interband absorption threshold for vanadium or paramagnetic chromium. Similar calculations in Ref. 6 revealed a threshold for rhodium and iridium of magnitude comparable to the spin-orbit splitting. We note that all of these calculations assume that the matrix elements are constant and therefore provide no information regarding the absolute value of $\tilde{\epsilon}(\omega)$; we will show below that the dependences $\tilde{\epsilon}(\omega)$ may therefore be quite unreliable. Moreover, the reasons for the different low-frequency behavior $\tilde{\epsilon}(\omega)$ for the different metals were not determined.

We will pause here briefly to discuss another discrepancy—the plasma frequencies for the transition metals deduced from the low-frequency experimental curves $\tilde{\epsilon}(\omega)$ lie below the values ω_p predicted by energy-band calculations, and the discrepancy is quite large, often 50–100% (see e.g., Ref. 9). Neither the error in the band calculations (which were accurate to within 10%) nor multielectron effects (which give a correction of ~ 5 –10% for the electron gas densities typical of the transition metals) can account for the disagreement. Although the anomalous skin effect, surface resistance, and (particularly) photon emission from excited electrons can greatly alter the collision frequency in pure metals and low temperature,¹⁰ they should have no effect on ω_p .

Although incomplete and contradictory, the above findings suggest that the dependence of the optical properties of transition metals is quite complicated at infrared frequencies. The crucial question is whether intense low-energy interband transitions are present. In order to find the answer, we have investigated the function $\tilde{\epsilon}_2(\omega)$ theoretically and calculated $\tilde{\epsilon}_2(\omega)$ numerically for the metals V, Nb, Mo, Rh, and Pd for $\hbar\omega \lesssim 0.7$ eV. Our combined analytic and nu-

meric analysis enabled us to identify and analyze in detail several typical situations in which $\tilde{\epsilon}_2(\omega)$ has peaks and valleys at low frequencies.

1. DEGENERACY OF THE ELECTRON SPECTRUM AND THE LOW-FREQUENCY INTERBAND CONDUCTIVITY OF METALS

In the random phase approximation, the imaginary part of the interband dielectric permittivity is given by

$$\tilde{\epsilon}_2(\omega)_{\alpha\beta} = \frac{4\pi^2 e^2}{m^2 \omega^2} \frac{1}{(2\pi)^3} \int d\mathbf{k} \sum_{\lambda \neq \lambda'} \langle \mathbf{k}\lambda | \hat{p}_\alpha | \mathbf{k}\lambda' \rangle \langle \mathbf{k}\lambda' | \hat{p}_\beta | \mathbf{k}\lambda \rangle \times f_{\mathbf{k}\lambda} (1 - f_{\mathbf{k}\lambda'}) \delta(\hbar\omega - E_{\lambda'}(\mathbf{k}) + E_\lambda(\mathbf{k})), \quad (3)$$

where \hat{p}_α is the α -component of the momentum operator, the integration is over all \mathbf{k} in the Brillouin zone, and $|\mathbf{k}\lambda\rangle$ are the one-electron states in the band labeled by λ [the band energies are $E_\lambda(\mathbf{k})$ and the occupation numbers are $f_{\mathbf{k}\lambda}$]. The interband dielectric permittivity is directly related by $\tilde{\sigma}(\omega) = \omega \tilde{\epsilon}_2(\omega) / 4\pi$ to the interband conductivity. We note that Eq. (3) does not suffice to describe direct interband transitions that involve photons, lattice defects, local field effects, etc. However, we will neglect these complications and base the analysis on Eq. (3). We may also use the approximation $f_{\mathbf{k}\lambda} \approx \theta[E_F - E_\lambda(\mathbf{k})]$, because the characteristic variations in $E_\lambda(\mathbf{k})$ in metals are much greater than kT for $T \lesssim 300$ K.

We will be interested only in low-frequencies $kT \lesssim \hbar\omega_D < \hbar\omega \lesssim 0.7$ eV, where ω_D is the Debye frequency of the phonons. In this case only transitions between electron states satisfying

$$E_\lambda(\mathbf{k}) \approx E_F \approx E_{\lambda'}(\mathbf{k}) \quad (4)$$

contribute to $\tilde{\epsilon}_2(\omega)$; here the symbol \approx denotes equality to within $\sim \hbar\omega$. Condition (4) is unlikely to be satisfied by chance for small $\hbar\omega$; this suggests that the low-frequency interband conductivity should be related to the degeneracy in the electronic spectrum.

We first consider the limit $\hbar\omega \rightarrow 0$. In this case the degeneracy of the electron spectrum at isolated points in the Brillouin zone is of little interest, because the probability that the energy of a degenerate level will be precisely equal to E_F is vanishingly small. Degeneracy of the bands along a line or a face of the Brillouin zone is more important; the degeneracy can only be two-fold if we neglect the spin. According to perturbation theory, the formula

$$E_{\lambda, \lambda'}(\mathbf{k}) = E_{\lambda, \lambda'}(\mathbf{k}_0) + \hbar(k - k_0)_\parallel (\mathbf{p}_{\lambda, \lambda'}^{\mathbf{k}_0} + \mathbf{p}_{\lambda, \lambda'}^{\mathbf{k}_0}) / 2m \pm \hbar |\mathbf{k} - \mathbf{k}_0| \times \{ [(\mathbf{p}_{\lambda, \lambda'}^{\mathbf{k}_0} - \mathbf{p}_{\lambda, \lambda'}^{\mathbf{k}_0}) \cdot \mathbf{n}]^2 + (\mathbf{p}_{\lambda, \lambda'}^{\mathbf{k}_0} \cdot \mathbf{n})^2 \}^{1/2} + O((\mathbf{k} - \mathbf{k}_0)^2) \quad (5)$$

describes the behavior of the degenerate bands λ and λ' near a point of degeneracy \mathbf{k}_0 . Here $\mathbf{p}_{\lambda, \lambda'}^{\mathbf{k}_0} = \langle \mathbf{k}_0 | \lambda | \hat{\mathbf{p}} | \mathbf{k}_0 | \lambda' \rangle$ and \mathbf{n} is the unit vector along $\mathbf{k} - \mathbf{k}_0$. If \mathbf{k} is also a point of band degeneracy for λ and λ' (i.e., a line or plane of degeneracy passes through \mathbf{k}), Eq. (5) shows that $\mathbf{p}_{\lambda, \lambda'}^{\mathbf{k}_0} \cdot \mathbf{n} = 0$ and $\mathbf{p}_{\lambda, \lambda'}^{\mathbf{k}_0} \cdot \mathbf{n} = \mathbf{p}_{\lambda, \lambda'}^{\mathbf{k}_0} \cdot \mathbf{n} = 0$. The projection of the vectors $\mathbf{k} - \mathbf{k}_0$, \mathbf{n} , and \mathbf{p} parallel and normal to these directions will be denoted by $(k - k_0)_\parallel, n_\parallel, p_\parallel$ and $(k - k_0)_\perp, n_\perp, p_\perp$, respectively. It is clear that $\mathbf{p}_{\lambda, \lambda'}^{\mathbf{k}_0}$ can be nonzero only if $(p_{\lambda, \lambda'}^{\mathbf{k}_0})_\perp \neq 0$.

We will now examine the contribution to $\tilde{\epsilon}_2(\omega)$ from degeneracy of the bands λ, λ' along a line in the Brillouin zone. By virtue of (4), we need only consider a neighborhood of the point \mathbf{k}_0 where the degenerate band crosses the Fermi level. Two cases can arise, depending on the crystal symmetry and the position of the degenerate line in the Brillouin zone: a) $(p_{\lambda, \lambda'})_\perp \neq 0$; b) $(p_{\lambda, \lambda'})_\perp = (p_{\lambda, \lambda'})_\parallel = 0$.

We will examine case a) first. The dispersion law is then linear in \mathbf{k} near the point \mathbf{k}_0 :

$$E_{\lambda, \lambda'}(\mathbf{k}) = E_F + \hbar(k - k_0)_\parallel v_\parallel \pm \hbar(\mathbf{k} - \mathbf{k}_0)_\perp v_\perp(\mathbf{n}_\perp). \quad (6)$$

For cubic crystals the dielectric permittivity $\tilde{\epsilon}_2(\omega) = \text{Tr}\{\tilde{\epsilon}_2(\omega)_{\alpha\beta}\} / 3$ is equal to

$$\tilde{\epsilon}_2(\omega \rightarrow 0) = \frac{1}{3} \frac{\hbar}{v_\parallel m a_B} \frac{1}{2\pi} \int d\mathbf{n}_\perp \left(\frac{p_{\lambda, \lambda'}^{\mathbf{k}_0}}{2m v_\perp(\mathbf{n}_\perp)} \right)^2, \quad (7)$$

where a_B is the Bohr radius. The limiting value $\tilde{\epsilon}_2(\omega \rightarrow 0)$ is nonzero because the factors ω^2 cancel in the numerator and denominator in (3) (the ω^2 in the numerator accounts for the volume of the phase region which contributes to $\tilde{\epsilon}_2$). Using the Kramers-Kronig dispersion relation, we readily find that $\epsilon_1(\omega) \sim \ln(\omega/\omega_0)$ as $\hbar\omega \rightarrow 0$, where ω_0 is the cutoff frequency.

Equation (5) implies that in case b) the degeneracy is lifted quadratically:

$$E_{\lambda, \lambda'}(\mathbf{k}) = E_F + \hbar(k - k_0)_\parallel v_\parallel + \hbar^2(\mathbf{k} - \mathbf{k}_0)_\perp^2 / 2m_{\lambda, \lambda'}(\mathbf{n}_\perp), \quad (8)$$

while $\mathbf{p}_{\lambda, \lambda'}^{\mathbf{k}_0}$ varies linearly: $|\mathbf{p}_{\lambda, \lambda'}^{\mathbf{k}_0}| = \hbar|\mathbf{k} - \mathbf{k}_0|_\perp \xi(\mathbf{n}_\perp)$. Here we have introduced the effective masses m_λ and $m_{\lambda'}$, which depend on the direction \mathbf{n}_\perp ; this is more convenient for our purposes than the more usual effective mass tensors. The low-frequency contribution for cubic crystals is equal to

$$\tilde{\epsilon}_2(\omega \rightarrow 0) = \frac{1}{3} \frac{\hbar}{v_\parallel m a_B} \frac{1}{2\pi} \int d\mathbf{n}_\perp \left[\frac{2m_\lambda(\mathbf{n}_\perp) m_{\lambda'}(\mathbf{n}_\perp) \xi(\mathbf{n}_\perp)}{m(m_{\lambda'}(\mathbf{n}_\perp) - m_\lambda(\mathbf{n}_\perp))} \right]^2. \quad (9)$$

In the case $\tilde{\epsilon}_2(\omega \rightarrow 0)$ is nonzero because the phase volume and $(p_{\lambda, \lambda'})_\perp^2$ are both $\propto \omega$; their product thus gives a factor ω^2 in the numerator in (3) which cancels the ω^2 in the denominator.

We will now give several examples of band degeneracy along lines in the Brillouin zone. Case a) above occurs for bcc and fcc metals along the third-order axis Λ (in the Λ_3 representation), and also along the third-order axis F (F_3 representation) in bcc metals (cf. Fig. 1). Random degeneracy of type a) can also occur if the line of degeneracy lies in a symmetry plane of the Brillouin zone or passes through points in general position (the latter can occur only in crystals with an inversion center, e.g., in bcc and fcc metals). Case b) occurs in bcc and fcc metals along a fourth-order axis Δ (the Δ_5 representation), cf. Fig. 1. No other degenerate lines can occur in the Brillouin zone for bcc and fcc metals. Figure 2 gives an idea of the frequency of degenerate lines in typical metals; the band structure for niobium (bcc) and rhodium (fcc) are shown.

Two bands can be degenerate at all points on a face of the Brillouin zone only if the system is symmetric under time

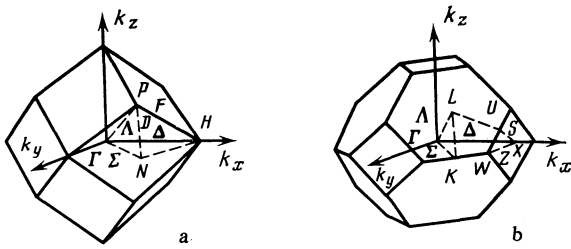


FIG. 1. The Brillouin zone: a) bcc lattice; b) fcc lattice. The symmetric lines and points are indicated.

reversal; in this case, the face must be normal to a second-order screw axis.¹¹ Since bcc and fcc crystals lack screw-axis symmetry, this type of degeneracy cannot occur. However, it is known that two-dimensional degeneracy can occur on the face of the Brillouin zone normal to the sixth-order axis in metals with a hexagonal closepacked (hcp) structure. We will now examine such metals in greater detail.

A group-theoretic analysis shows that $(p_{\lambda\lambda'}^{k_0})_{\perp} \neq 0$ on the face of the Brillouin zone normal to the sixth-order axis in hcp metals, so that the degeneracy is lifted linearly as the point \mathbf{k} moves away from the face. Only the neighborhood of the line L where the face intersects the Fermi surface is of interest for infrared optics; in this neighborhood the dispersion equation is of the form

$$E_{\lambda, \lambda'}(\mathbf{k}) = E_F + \hbar(\mathbf{k} - \mathbf{k}_0)_{\parallel} (p_{\lambda\lambda'}^{k_0})_{\parallel} / m \pm \hbar(\mathbf{k} - \mathbf{k}_0)_{\perp} v_{\perp}(\mathbf{k}_0), \quad (10)$$

where the point \mathbf{k}_0 is assumed to lie on L . The corresponding contribution to $\tilde{\epsilon}_2$ is anisotropic:

$$\tilde{\epsilon}_2(\omega \rightarrow 0)_{zz} = \frac{1}{\pi} \oint_{(L)} \frac{dl_{\mathbf{k}_0} \hbar^2}{\hbar \omega m a_B} \frac{(p_{\lambda\lambda'}^{k_0})^2}{2m v_{\perp}(\mathbf{k}_0) |p_{\lambda\lambda'}^{k_0}|_{\parallel}}, \quad (11)$$

on the other hand, $\epsilon_2(\omega \rightarrow 0)_{z\alpha} = \text{const}$ and $\tilde{\epsilon}_2(\omega \rightarrow 0)_{\alpha\alpha} \propto \omega$, where the z axis lies along the sixth-order axis normal to the face, and $\alpha = x, y$. This behavior of $\tilde{\epsilon}_{2zz}$ is a consequence of the fact that the phase volume in this case is $\propto \hbar\omega$, so that one of the factors ω cancels in the denominator (3). As a consequence, $\tilde{\epsilon}_{2zz} \sim 1/\omega$ and $\tilde{\sigma}_{zz}(\omega \rightarrow 0) = \text{const}$. One can show by using the Kramers-Kronig dispersion relation that in addition, $\tilde{\epsilon}_1(\omega \rightarrow 0) = \tilde{\epsilon}_0 > 0$. Our numerical estimates indicates that $\tilde{\sigma}_{zz}$ may be as large as $\sim 10\%$ of the Drude intraband conductivity. It is readily seen from the form of their Fermi surfaces^{12,13} that a similar contribution to $\tilde{\epsilon}_2$ may be expected for virtually all hcp metals.

Our analysis thus far has been limited to the nonrelativistic approximation, and the spin-orbit interaction has been neglected. The latter is known to remove the degeneracy along the Λ and Δ axes in bcc and fcc metals; in addition, the degeneracy along the F axis in bcc metals is also lifted. In hcp metals the spin-orbit interaction lifts the degeneracy on the face of the Brillouin zone everywhere except on the line AL joining the center of the face to the midpoint of an edge. The magnitude of the splitting for the $3d$ -transition metals is at most 0.02 eV, i.e., $\sim \hbar\omega_D$; it can reach ~ 0.1 eV and ~ 0.5 eV in the $4d$ - and $5d$ -transition metals, respectively, although it may be considerably less at certain points in the Brillouin zone. The spin-orbit interaction can therefore be neglected in $3d$ -metals and their compounds but should probably be included for the $4d$ -metals, even though this is not always necessary. The spin-orbit interaction can appreciably alter the low-frequency interband conductivity in $5d$ -metals.

For the one- and two-dimensional band degeneracies considered above, the limit $\tilde{\epsilon}_2(\omega \rightarrow 0)$ is nonzero and the interband contribution depends monotonically on the frequency. In order to understand the features of the electron spectrum that are responsible for the nonmonotonic dependence $\tilde{\epsilon}_2(\omega)$ at low frequencies $\hbar\omega \sim 0.1-0.3$ eV, we will examine the case when an energy level is degenerate at a point \mathbf{k}_0 of high symmetry in the Brillouin zone and lies at a distance $\sim \hbar\omega$ from the Fermi surface E_F . We have $p_{\lambda\lambda}^{k_0} = 0$ for degenerate levels and $p_{\lambda\lambda'}^{k_0} = 0$ for degenerate bands at such points in bcc and fcc metals. According to (5), the dispersion law for degenerate bands λ and λ' near \mathbf{k}_0 is quadratic,

$$E_{\lambda, \lambda'}(\mathbf{k}) = E_{\lambda, \lambda'}(\mathbf{k}_0) + \hbar^2(\mathbf{k} - \mathbf{k}_0)^2 / 2m_{\lambda, \lambda'}(\mathbf{n}) \quad (12)$$

and $|p_{\lambda\lambda'}^{k_0}| = \hbar|\mathbf{k} - \mathbf{k}_0| \xi(\mathbf{n})$. Two fundamentally different cases (sketched in Fig. 3) can occur: a) m_{λ} and $m_{\lambda'}$ have the same signs; b) m_{λ} and $m_{\lambda'}$ have opposite signs. It is clear from Fig. 3a that for case a), the interband absorption begins at energy $\hbar\omega_1$ and ends at $\hbar\omega_2$; this nonmonotonic behavior may clearly cause a peak in the $\tilde{\epsilon}_2(\omega)$ curve. For case b) (Fig. 3b) the absorption has a threshold character—it begins at $\hbar\omega_1$ and persists to high energies. In analytic form, the result for cubic crystals can be expressed as

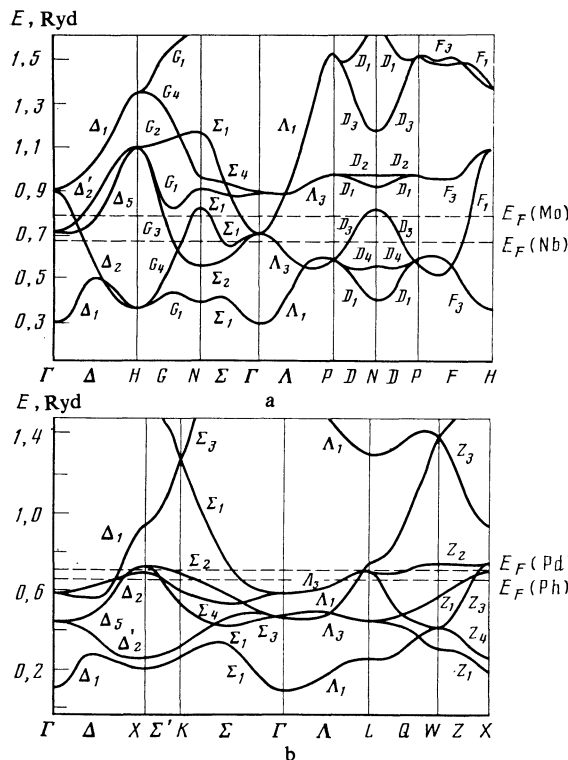


FIG. 2. Band structure: a) niobium (bcc lattice); b) rhodium (fcc). The dashed lines show the approximate positions of the Fermi surface E_F for molybdenum and palladium.

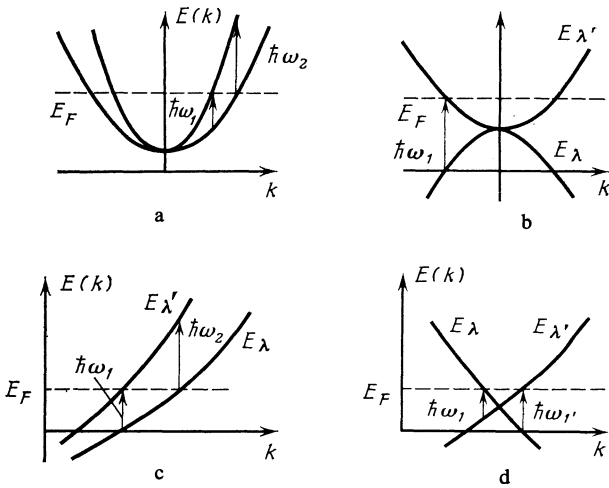


FIG. 3. Sketch of band structure. Near a point of high symmetry: a) $m_\lambda > m_{\lambda'} > 0$; b) $m_{\lambda'} > 0 > m_\lambda$; near a general point in the Brillouin zone: c) $v_\lambda(\mathbf{k})v_{\lambda'}(\mathbf{k}) > 0$; d) $v_\lambda(\mathbf{k})v_{\lambda'}(\mathbf{k}) < 0$.

$$\tilde{\epsilon}_2(\omega) = \int_{m_\lambda(\mathbf{n}) \geq m_{\lambda'}(\mathbf{n}) > 0} d\mathbf{n} A(\mathbf{n}) \theta\left(\hbar\omega - \Delta \frac{m_\lambda(\mathbf{n}) - m_{\lambda'}(\mathbf{n})}{m_\lambda(\mathbf{n})}\right) \times \theta\left(\Delta \frac{m_\lambda(\mathbf{n}) - m_{\lambda'}(\mathbf{n})}{m_{\lambda'}(\mathbf{n})} - \hbar\omega\right), \quad (13)$$

$$\tilde{\epsilon}_2(\omega) = \int_{m_{\lambda'}(\mathbf{n}) > 0 > m_\lambda(\mathbf{n})} d\mathbf{n} A(\mathbf{n}) \theta\left(\hbar\omega - \Delta \frac{m_{\lambda'}(\mathbf{n}) - m_\lambda(\mathbf{n})}{|m_\lambda(\mathbf{n})|}\right), \quad (14)$$

$$A(\mathbf{n}) = \frac{1}{12\pi} \left(\frac{\hbar^2}{m a_B^2 \hbar\omega}\right)^{3/2} \frac{m_{\lambda'}^2(\mathbf{n}) m_\lambda^2(\mathbf{n}) \xi(\mathbf{n})}{(m_\lambda(\mathbf{n}) - m_{\lambda'}(\mathbf{n}))^2 m^2} \times \left[\frac{m_\lambda(\mathbf{n}) m_{\lambda'}(\mathbf{n})}{m(m_\lambda(\mathbf{n}) - m_{\lambda'}(\mathbf{n}))}\right]^{1/2}, \quad (15)$$

where we have assumed that $\Delta = E_F - E_{\lambda, \lambda'}(\mathbf{k}_0) > 0$. The other cases (e.g., $\Delta < 0$ and $m_\lambda < m_{\lambda'} < 0$) follow easily from (13)–(15) by changing the signs. It should be noted that the symmetry of the point \mathbf{k}_0 in the Brillouin zone has no influence on whether the contribution is described by (13) or (14). Moreover, in some cases $m_\lambda(\mathbf{n})$ and $m_{\lambda'}(\mathbf{n})$ may have the same sign along one direction but opposite signs along another. The behavior of $\tilde{\epsilon}_2(\omega)$ associated with the total contribution from a neighborhood of a point of high symmetry may therefore be quite diverse; in particular, $\tilde{\epsilon}_2(\omega)$ may have a maximum.

The above situation in which $\tilde{\epsilon}_2(\omega)$ is nonmonotonic is not as exceptional as might appear at first sight. For instance, bcc metals have six levels which are doubly or triply degenerate near points of high symmetry at optical frequencies. A similar type of degeneracy also occurs in fcc metals (Fig. 2). Since we are interested in situations when E_F lies within $\hbar\omega \sim 0.3$ eV from one of the degenerate levels, and the latter comprise approximately 1/3 of the width of the d -band, $\tilde{\epsilon}_2(\omega)$ is quite likely to contain significant contributions of the type (13) or (14).

We note that contributions similar to (13) and (14) can also arise near a general point in the Brillouin zone if two sheets of the Fermi surface approach each other closely near

the point. The situation shown in Fig. 3c correspond to the case when the velocities of the electrons on the sheets λ and λ' are almost parallel [$v_\lambda(\mathbf{k})v_{\lambda'}(\mathbf{k}) > 0$]; in this case $\tilde{\epsilon}_2(\omega)$ has a minimum of the form (13). If the velocities are antiparallel: $v_\lambda(\mathbf{k})v_{\lambda'}(\mathbf{k}) < 0$ (Fig. 3d), $\tilde{\epsilon}_2(\omega)$ has a threshold dependence (14). The primary difference from the case of degeneracy near points of high symmetry is that the approximate equality $E_{\lambda'}(\mathbf{k}) \approx E_\lambda(\mathbf{k})$ near a general point is fortuitous and cannot be predicted by symmetry arguments.

2. NUMERICAL STUDY OF THE OPTICAL PROPERTIES OF bcc AND fcc TRANSITION METALS

In the previous section we examined several types of electron degeneracy typical in infrared optics. It would be desirable to find out how common these situations are and the extent to which the above analysis can be applied to specific metals. We therefore calculated $\tilde{\epsilon}_2(\omega)$ numerically in the nonrelativistic case for vanadium, niobium, and molybdenum (bcc lattice) and for rhodium and palladium (fcc lattice). The technique described in Ref. 14 was used in the calculation, which was based on Eq. (3). This method was previously employed in Refs. 14 and 15 to calculate $\epsilon(\omega)$ and the reflection coefficient for a wide range of frequencies and gave results in close agreement with experiment.

Only the localized regions where (4) holds (not the entire Brillouin zone) contribute to $\tilde{\epsilon}_2(\omega)$ at infrared frequencies; this was responsible for some specific features of the calculation. First, the error in $\tilde{\epsilon}_2(\omega)$ was determined not by the average computational error for the band structure but by the error in the position of a few individual band relative to E_F . This error is ≈ 0.1 eV for *ab initio* calculations such as ours. Second, the constant-matrix-element approximation breaks down completely, because $|\mathbf{p}_{\lambda\lambda'}^{\mathbf{k}}| = 0$ at numerous points and lines of high symmetry. We therefore avoided this approximation. Third, in order to facilitate the integration over k in (3) it is helpful to first identify the \mathbf{k} values in the Brillouin zone that contribute to $\tilde{\epsilon}_2(\omega)$ and then integrate only over them. We used the tetrahedral technique¹⁶ to perform the numerical integration. In order to achieve $\sim 10\%$ accuracy, a rather small mesh size was necessary (from 1500 to as many as $\sim 10,000$ \mathbf{k} -points in a region comprising 1/48 of the volume of the Brillouin zone).

The calculated results are summarized in Table I, which analyzes the behavior of $\tilde{\epsilon}_2(\omega)$ in the limit $\omega \rightarrow 0$. The coordinates of the points \mathbf{k}_0 contributing to $\tilde{\epsilon}_2(\omega)$ as $\hbar\omega \rightarrow 0$, the nature of the degeneracy, and the magnitude of the contribution $\tilde{\epsilon}_2(\omega \rightarrow 0)$ are given. At least one instance of one-dimensional degeneracy was found for each of the five metals investigated, which indicates that this phenomenon may be common.

Figure 4 shows the calculated curves $\tilde{\epsilon}_2(\omega)$ for the five metals. We will now investigate which features of the electron structure are responsible for the peaks in $\tilde{\epsilon}_2(\omega)$ for each of the metals. Vanadium and niobium are group VA elements and have similar band structures and Fermi surfaces. The band structure shown in Fig. 2a suggests that the peak in $\tilde{\epsilon}_2(\omega)$ is associated with $\Sigma_2 \rightarrow \Sigma_1$ transitions, which are very similar to the interband transitions in Fig. 3a. The two bands

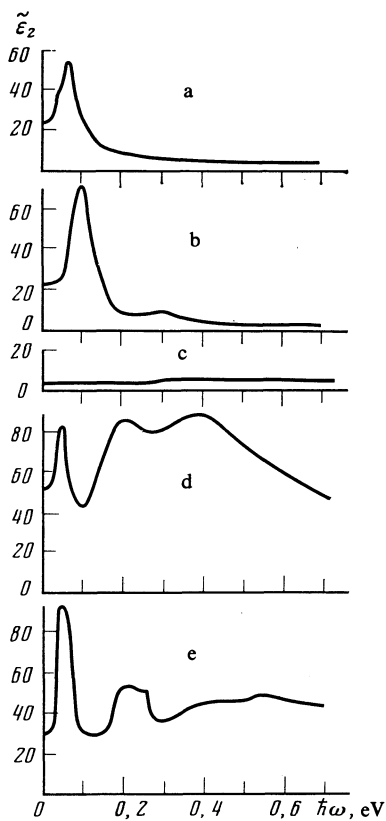


FIG. 4. Calculated curves $\tilde{\epsilon}_2(\omega)$ for vanadium (a), niobium (b), molybdenum (c), rhodium (d), and palladium (e).

coalesce in the Λ direction but lie above E_F along the Δ direction. In order to study the band behavior for intermediate directions, we consider the curves formed by the intersection of the Fermi surface with the planes of high symmetry (Fig. 5). Band Σ_2 corresponds to a hole surface in the second band near the point Γ (an "octahedron"), while band Σ_1 correspond to a tubular perforated surface in the third band along the direction ΓH ("playground jungles"). The calculation shows that the chief contribution to $\tilde{\epsilon}_2(\omega)$ comes from the region where the surfaces h_2 and e_3 approach and touch, and, especially, from the neighborhoods of the two points of random degeneracy (Table I). The latter regions are responsible for the peak in $\tilde{\epsilon}_2(\omega)$.

The calculated curve $\tilde{\epsilon}_2(\omega)$ for niobium agrees reasonably well with available experimental data. The principal maximum at $\hbar\omega = 0.09$ eV (Fig. 4) corresponds to the

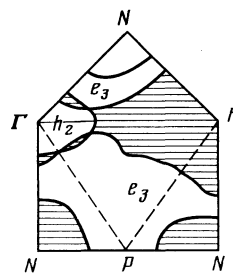


FIG. 5. Intersections of the Fermi surface for niobium with planes of high symmetry.

abrupt peak at $\hbar\omega \approx 0.1$ eV found in Ref. 3. However, the absolute magnitude of the peak is smaller—our calculation implies a peak value of 70, whereas the estimates in Ref. 3 give 200–300. The weak maximum at $\hbar\omega = 0.3$ eV (Fig. 4) can in principle be identified with the experimental maximum in $\tilde{\epsilon}_2(\omega)$ found in Ref. 1 at the same frequency, although the peak there was sharper and roughly three times as high.

The analysis of the band structure (Fig. 2a) and Fermi surface^{12,13} for molybdenum suggest that $\tilde{\epsilon}_2(\omega)$ will be monotonic; this is confirmed by the numerical calculation (Fig. 4c) and by the experimental findings in Ref. 3.

The most complicated situation occurs for rhodium. The band structure (Fig. 2b) and the curves where the bands cross the Fermi surface (Fig. 6) suggest that two regions in k -space should give the dominant contribution to $\tilde{\epsilon}_2(\omega)$. The first region contains the point X , where the geometry of the imbedded hole surfaces in the third and fourth bands ("ellipsoids") is very similar to the situation shown in Fig. 3a. The chief difference is that the bands X_2 and X_3 are non-degenerate, so that the matrix element $|\mathbf{p}_{\lambda\lambda}^k| \neq 0$ at the point X . The large electron surface in the sixth band near the point Γ and the tubular perforated surface (elongated along the LX direction) approach each other closely along the line LX , which forms the axis of the second region (this approach is "random" and cannot be predicted from symmetry arguments). These two regions are responsible for the low-frequency peaks in $\tilde{\epsilon}_2(\omega)$ at $\hbar\omega = 0.05$ eV, and for the two principal peaks at 0.21 and 0.4 eV. Similar peaks in the optical conductivity were noted experimentally in Ref. 6, where a pronounced maximum at $\hbar\omega = 0.07$ eV was followed by dip at 0.13 eV, corresponding to the minimum in the calculated curve at $\hbar\omega = 0.11$ eV; the peaks at $\hbar\omega = 0.2$ and 0.4 eV were also observed.¹⁾ The experimental dependence $\sigma(\omega)$ found

TABLE I.

Metal	$k_0, 4\pi/a$	Type of degeneracy	$\tilde{\epsilon}_2(\omega \rightarrow 0)$	$\tilde{\epsilon}_2(\omega \rightarrow 0)$ total
V	(0.072; 0.072; 0.072)	Regular	3.0	24.6
	(0.134; 0.049; 0.049)	Random	21.6	
	(0.159; 0.063; 0)			
Nb	(0.056; 0.056; 0.056)	Regular	3.2	23.4
	(0.136; 0.033; 0.033)	Random	20.2	
	(0.156; 0.043; 0)			
Mo	(0.255; 0; 0)	Regular	4.1	4.1
Rh	(0.365; 0; 0)	Regular	44.9	51.2
	(0.185; 0.185; 0.185)	Regular	6.3	
Pd	(0.403; 0; 0)	Regular	29.0	29.0

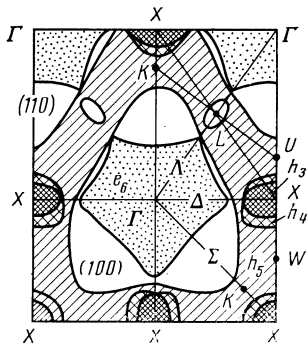


FIG. 6. Intersections of planes of high symmetry with the Fermi surface for rhodium.

in Ref. 19 shows the same basic behavior: the interband conductivity has a minimum at $\hbar\omega = 0.13$ eV and maxima at $\hbar\omega \approx 0.2$ and 0.35 eV. On the other hand, the calculation gives no hint of the weak peaks at 0.10 and 0.14 eV in the optical conductivity that were detected in Ref. 16.

Analysis of the band structure (Fig. 2b) and Fermi surface (Refs. 12 and 13) for palladium reveals that any sharp peaks in $\tilde{\epsilon}_2(\omega)$ in this case must originate from a neighborhood of the point X. Our calculation (Fig. 4e) shows that the peaks at $\hbar\omega = 0.05$ and 0.22 eV are in fact due to X. The gentle maximum for $\hbar\omega \approx 0.5$ eV is caused by transitions between the fifth and sixth bands near the boundary of the large sheet of the Fermi surface surrounding the point Γ . According to the experimental results in Ref. 20, the most important features of $\sigma(\omega)$ for palladium were sharp rise at 0.15 eV and a peak of 0.19 eV, which are in excellent agreement with our results. Although the peak at $\hbar\omega \approx 0.5$ eV found in Ref. 16 occurs at roughly the same energy as the peak in the theoretical curve, it is much sharper.

We will now pause to discuss how the low-frequency interband transitions affect the accuracy in determining the plasma and collision frequencies ω_p and γ that characterize the Drude conductivity. Equation (1) gives the imaginary part of $\epsilon(\omega)$, while the real part is equal to

$$\epsilon_1(\omega) = 1 - \frac{\omega_p^2}{\omega^2 + \gamma^2} + \tilde{\epsilon}_1(\omega), \quad (16)$$

where $\tilde{\epsilon}_1(\omega)$ and $\tilde{\epsilon}_2(\omega)$ are related by the Kramers-Kronig formula

$$\tilde{\epsilon}_1(\omega) = \frac{2}{\pi} \int \frac{\omega_1 \tilde{\epsilon}_2(\omega_1)}{(\omega_1^2 - \omega^2)} d\omega_1. \quad (17)$$

If there are no low-frequency interband transitions then $\tilde{\epsilon}_2(\omega) = 0$ and $\tilde{\epsilon}_1(\omega) \approx \text{const}$ at infrared frequencies. If we plot

$1 - \epsilon_1(\omega)$ and $\omega\epsilon_2(\omega)$ as functions of $(\omega_2 + \gamma_2)^{-1}$ and $1 + \tilde{\epsilon}_0 - \epsilon_1(\omega)$, respectively, we will then get straight lines or slope ω_p^2 and γ . These plots (called Argand diagrams) are widely used to find ω_p and γ from the experimental curves²⁾ $\epsilon(\omega)$.

In order to understand the qualitative effects of the interband transitions, we analyzed the experimental curves as usual by theoretically plotting the Argand diagrams for each of the five metals for $0.05 \text{ eV} \leq \hbar\omega \leq 0.7 \text{ eV}$. We used Eqs. (1)–(3), (16), (17) to calculate $\epsilon(\omega)$, and the theoretical values of ω_p and γ were taken from Ref. 17 (Table II). The table shows that the calculated values for ω_p and γ are generally substantially higher than the experimental values, although there is reasonably good agreement in a few cases.

However, the actual form of the Argand diagrams is of greater interest. Figure 7 shows the diagrams calculated for niobium. Both of the dependences are linear for $\hbar\omega \geq 0.35$ eV, where the interband transitions are weak. The values of ω_p and γ deduced from the slopes of the lines differ from the original values by 6% and 15%, respectively. The interband transitions are important for $\hbar\omega < 0.35$ eV, and in this region the curves are essentially nonlinear, so that ω_p and γ depend strongly on the frequency. Thus, the plasma frequency deduced from our Argand diagrams for $0.15 \text{ eV} \leq \hbar\omega \leq 0.35 \text{ eV}$ increases from 5 to 27 eV as $\hbar\omega$ decreases, in qualitative agreement with the experimental frequency dependence $\hbar\omega_p(\hbar\omega)$ found in Ref. 3. Accurate determinations of ω_p and γ are scarcely possible for these energies. The form of the Argand diagrams for the other metals is similar—they are nearly straight lines $\tilde{\epsilon}_2(\omega)$ varies slowly, but their complicated nonlinear behavior where $\tilde{\epsilon}_2(\omega)$ varies rapidly makes it impossible to determine ω_p and γ accurately. Of the five metals investigated, only molybdenum has a straight-line Argand diagram for all frequencies (this is due partly to the small magnitude of $\tilde{\epsilon}_2(\omega)$, but primarily to the fact that it varies slowly). The linearity of the Argand diagrams for molybdenum was also noted experimentally in Ref. 3.

CONCLUSIONS

The crystal symmetry (more precisely, the degeneracy of the electron spectrum) has a very great influence on the low-frequency interband conductivity. It is the rule rather than the exception for cubic and hexagonal metals to have “zerogap” interband transitions with $\tilde{\epsilon}_2(\omega \rightarrow 0) = \text{const}$ and $\tilde{\epsilon}_2(\omega \rightarrow 0) \sim 1/\omega$, respectively. Contrary to widespread opinion, the curves $\tilde{\epsilon}_2(\omega)$ at infrared frequencies generally have well-defined structure with thresholds or peaks. Our numerical studies reveal that values $\tilde{\epsilon}_2(\omega) \sim 1 \cdot 10^1 - 1 \cdot 10^2$ are

TABLE II.

	V	Nb	Mo	Rh	Pd
$\hbar\omega_p$ th eV	8.07	9.84	9.28	9.77	6.94
$\hbar\omega_p$ exp. eV	{ 4.92 [3] 5.29 [18]	{ 7.91 [1] 7.21 [3]	{ 5.78 [3]	{ 4.16 [8] 5.19 [19]	{ 5.67 [16] 2.77 [19]
$\hbar\gamma$ th. eV	0.940	0.950	0.304	0.298	0.344
$\hbar\gamma$ exp. eV	{ 0.495 [3] 0.203 [18]	{ 0.940 [1] 0.929 [3]	{ 0.349 [3]	{ 0.206 [8] 0.102 [19]	{ 0.185 [16] 0.068 [19]

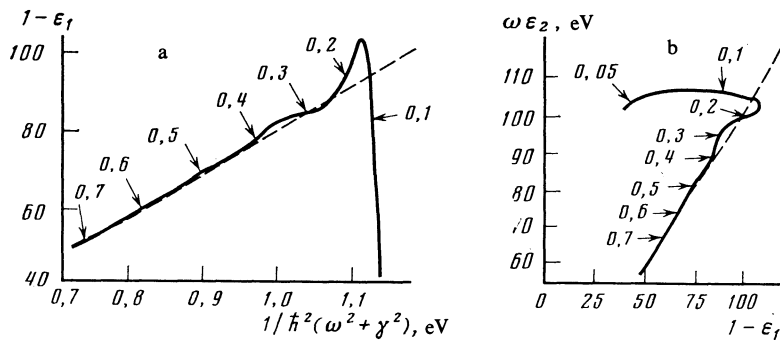


FIG. 7. Calculated Argand diagrams for niobium: a) $1 - \epsilon_1(\omega)$ as a function of $[\hbar^2(\omega^2 + \gamma^2)]^{-1}$; b) $\omega\epsilon_2(\omega)$ as a function of $1 - \epsilon_1(\omega)$. The numbers alongside the curves give the energies $\hbar\omega$ in eV; the dashed lines correspond to $\hbar\omega_p = 10.4$ eV and $\hbar\gamma = 0.8$ eV.

typical for cubic crystals at IR frequencies. The interband conductivity may appear to be of minor importance compared to the intraband conductivity that dominates at low frequencies—the ratio $\bar{\sigma}/\sigma$ is $\lesssim 5\%$ for $\hbar\omega \sim 0.1$ – 0.2 eV, and the interband transitions change the reflection coefficient by only 0.1–1.0%. However, even at this level the interband transitions can seriously complicate the determination of ω_p and γ from the experimental curves $\epsilon(\omega)$.

We thank A. I. Golovashkin, E. G. Maksimov, and G. P. Motulevich for conversations illuminating various aspects of the problem, and M. M. Kirillova for drawing our attention to this topic.

¹The minimum at $\hbar\omega = 0.2$ eV was not specifically discussed in Ref. 6 but shows up clearly in the wavelength dependences $n(\lambda)$, $k(\lambda)$ for the optical constants.

²As usual, we have assumed that $\bar{\epsilon}_0 = 0$ in our analysis of the results.

¹A. I. Golovashkin, I. E. Leksina, G. P. Motulevich, and A. A. Shubin, *Zh. Eksp. Teor. Fiz.* **56**, 51 (1969) [*Sov. Phys. JETP* **29**, 27 (1969)].

²J. H. Weaver, D. W. Lynch, and C. G. Olson, *Phys. Rev.* **B7**, 4311 (1973).

³M. M. Kirillova and L. V. Nomerovannaya, *Fiz. Tverd. Tela* **20**, 984 (1978) [*Sov. Phys. Solid State* **20**, 568 (1978)].

⁴J. H. Weaver, D. W. Lynch, and C. G. Olson, *Phys. Rev.* **B10**, 501 (1974).

⁵J. H. Weaver, *Phys. Rev.* **B11**, 1416 (1975).

⁶V. G. Topol'skiĭ, V. P. Shirokovskii, M. M. Kirillova, and L. V. Nomerovannaya, *Fiz. Met. Metalloved.* **52**, 745 (1981).

⁷W. E. Pickett and P. B. Allen, *Phys. Rev.* **B11**, 3599 (1975).

⁸G. V. Ganin, M. M. Kirillova, L. V. Nomerovannaya, and V. P. Shirokovskii, *Fiz. Met. Metalloved.* **43**, 907 (1977).

⁹A. G. Veprev and V. P. Shirokovskii, *Fiz. Met. Metalloved.* **48**, 19 (1979).

¹⁰G. P. Motulevich, *Usp. Fiz. Nauk* **97**, 211 (1969) [*Sov. Phys. Uspekhi* **12**, 80 (1969)].

¹¹C. Herring, *Phys. Rev.* **52**, 361 (1937).

¹²A. P. Cracknell and K. C. Wong, *Fermi Surface: Its Concept, Determination and Use in Physics of Metals*, Clarendon Press, Oxford (1973).

¹³Landolt-Bornstein. New Series, Group III, vol. 13, subvol. B (1983).

¹⁴Yu. A. Uspenskiĭ, E. G. Maksimov, S. N. Rashkeev, and I. I. Mazin, *Z. Phys. B: Condensed Matter* **53**, 263 (1983).

¹⁵Yu. A. Uspenskiĭ, S. N. Rashkeev, and I. I. Mazin, in: *Proc. Thirteenth Ann. Int. Symp. Electronic Structures of Metals and Alloys, Dresden (1983)*, p. 52.

¹⁶Zh. Duĭsebaeva, M. I. Korsunskii, and G. P. Motulevich, *Opt. Spektrosk.* **34**, 535 (1973) [*Opt. Spectrosc. (USSR)* **34**, 307 (1973)].

¹⁷I. I. Mazin, E. M. Savitskii, and Yu. A. Uspenskii, *J. Phys. F: Metal Physics* **14**, 167 (1984).

¹⁸A. I. Golovashkin, I. D. Mash, and G. P. Motulevich, *Kratk. Soob. po Fiz.*, No. 9, 51 (1970).

¹⁹G. A. Bolotin and T. P. Chukina, *Opt. Spektrosk.* **23**, 620 (1967) [*Opt. Spectrosc. (USSR)* **23**, 333 (1967)].

²⁰G. A. Bolotin, M. M. Kirillova, L. V. Nomerovannaya, and M. M. Noskov, *Fiz. Met. Metalloved.* **23**, 463 (1967).

Translated by A. Mason